

## Accretion properties of MAXI J1813–095 during its failed outburst in 2018

Arghajit Jana<sup>1</sup>, Gaurava K. Jaisawal<sup>2</sup>, Sachindra Naik<sup>1</sup>, Neeraj Kumari<sup>1,4</sup>, Debjit Chatterjee<sup>5,3</sup>, Kaushik Chatterjee<sup>3</sup>, Riya Bhowmick<sup>3</sup>, Sandip K. Chakrabarti<sup>3</sup>, Hsiang-Kuang Chang<sup>6</sup> and Dipak Debnath<sup>3</sup>

<sup>1</sup> Astronomy & Astrophysics Division, Physical Research Laboratory, Navrangpura, Ahmedabad 380009, India; [argha0004@gmail.com](mailto:argha0004@gmail.com)

<sup>2</sup> National Space Institute, Technical University of Denmark, Elektrovej, 327-328, DK-2800 Lyngby, Denmark

<sup>3</sup> High Energy Astrophysics, Indian Centre for Space Physics, Garia St Road, Kolkata 700084, India

<sup>4</sup> Department of Physics, Indian Institute of Technology, Gandhinagar 382355, Gujarat, India

<sup>5</sup> Indian Institute of Astrophysics, Koramangala, Bangalore 560034, India

<sup>6</sup> Department of Physics, “National Tsing Hua University”, Hsinchu 30013, China

Received 2020 November 9; accepted 2020 December 31

**Abstract** We present the results obtained from detailed timing and spectral studies of a black hole candidate MAXI J1813–095 using *Swift*, *NICER*, and *NuSTAR* observations during its 2018 outburst. The timing behavior of the source is mainly studied by examining *NICER* light curves in the 0.5 – 10 keV range. We did not find any signature of quasi-periodic oscillations in the power density spectra of the source. We carry out spectral analysis with a combined disk blackbody & power law model, and physical two-component advective flow (TCAF) model. From the combined disk blackbody & power-law model, we extracted thermal and non-thermal fluxes, photon index and inner disk temperature. We also find evidence for weak reflection in the spectra. We have tested the physical TCAF model on a broadband spectrum from *NuSTAR* and *Swift*/XRT. The parameters like mass accretion rates, the size of Compton clouds and the shock strength are extracted. Our result affirms that the source remained in the hard state during the entire outburst which indicates a ‘failed’ outburst. We estimate the mass of the black hole as  $7.4 \pm 1.5 M_{\odot}$  from the spectral study with the TCAF model. We apply the LAOR model for the Fe  $K\alpha$  line emission. From this, the spin parameter of the black hole is ascertained as  $a^* > 0.76$ . The inclination angle of the system is estimated to be in the range of  $28^{\circ} - 45^{\circ}$  from the reflection model. We find the source distance to be  $\sim 6$  kpc.

**Key words:** X-Rays: binaries — stars individual: (MAXI J1813-095) — stars: black holes — accretion, accretion disks – shock waves — radiation: dynamics

### 1 INTRODUCTION

Transient black hole (BH) X-ray binaries (BHXRBs) occasionally manifest outbursts that last from weeks to months. During such an outburst, the X-ray intensity of the source rises thousands of times as compared to that during the quiescent state. An outburst is believed to be triggered when the viscosity is suddenly enhanced at the pileup radius (Chakrabarti 1990, 1996; Chakrabarti et al. 2019; Bhowmick et al. 2020). A transient BHXRB is known to exhibit characteristic evolution in the spectral and timing properties during these outbursts that are broadly classified as Type 1 and Type 2 outbursts (Debnath et al. 2017).

In case of Type 1 outbursts, BHXRBs display all the usual spectral states, viz., hard, hard-intermediate, soft-intermediate and soft states due to which these outbursts are called full or complete outbursts. On the other hand, in case of Type 2 outbursts, which are also known as failed outbursts, only harder spectral states (hard and hard-intermediate) are observed (Del Santo et al. 2016; Tetarenko et al. 2016; García et al. 2019).

In general, the spectrum of a BHXRB can be modeled with a power law (PL) continuum model along with a thermal multicolor disk blackbody (DBB) component. In addition, an Fe  $K\alpha$  emission line around  $\sim 6.4$  keV is observed (Remillard & McClintock 2006). It is believed

that the DBB component originates from a standard geometrically thin accretion disk (Shakura & Sunyaev 1973) whereas the PL component arises from a Compton cloud that consists of hot electrons (Sunyaev & Titarchuk 1980). The soft photons from the standard accretion disk are inverse Comptonized at the Compton cloud and produce a hard power-law tail. Several theoretical models have been developed in the literature to explain the nature of the Compton cloud (Zdziarski et al. 1993; Haardt & Maraschi 1993; Esin et al. 1997).

The Two-Component Advective Flow (TCAF) model is a generalized accretion flow solution where the transonic flow includes rotation, viscosity and radiative transfer. It can explain the observed spectral and timing properties of BHXRBs self-consistently (Chakrabarti & Titarchuk 1995; Chakrabarti 1997). In this model, the accretion flow has two components: a highly viscous Keplerian disk with high angular momentum, and a low viscous sub-Keplerian halo which has low angular momentum. The Keplerian disk is submerged within the sub-Keplerian flow and moves slowly in the equatorial plane. The sub-Keplerian flow forms an axisymmetric shock at the centrifugal boundary. The post-shock region consists of hot electrons and is known as CENBOL or CENtrifugal pressure supported BOundary Layer (Chakrabarti 1996). The CENBOL acts as a Compton cloud. The soft photons originate from the Keplerian disk and contribute to the multicolor blackbody component. A fraction of the soft photons are intercepted by the CENBOL, and get inverse-Comptonized and become hard photons that form the hard power-law tail. A fraction of the hard photons is reprocessed at the Keplerian disk and a ‘reflection hump’ is observed at higher energy. In the TCAF paradigm, quasi-periodic oscillations (QPOs) which are observed in power density spectra (PDSs) are produced by oscillation of the CENBOL (Molteni et al. 1996). The CENBOL is also the launch site of the jet. In recent years, the TCAF model has been utilized successfully to study the spectral and timing properties of several BHs and active galactic nuclei (Mondal et al. 2016; Chatterjee et al. 2016; Shang et al. 2019; Nandi et al. 2019; Chatterjee et al. 2020; Banerjee et al. 2020).

Black hole candidate (BHC) MAXI J1813–095 was discovered on 2018 February 19 (Kawase et al. 2018) with MAXI/GSC. Follow up observations with the *Swift*/XRT localized the source at RA = 18<sup>h</sup> 13<sup>m</sup> 34.0<sup>s</sup>, Dec = –09° 31′ 59″.0 (Kennea et al. 2018). The GROND observation of the above location detected the optical counterpart of the source (Rau 2018). The ATCA observation revealed a compact jet and classified the source as a radio-quiet

BHXRB (Russell et al. 2018). From the multi-wavelength observations, Armas Padilla et al. (2019) suggested that the companion star could be a G5V star with a distance of > 3 kpc.

In this paper, we studied MAXI J1813–095 in broad energy bands by relying on *Swift*/XRT, *NICER* and *NuSTAR* observations performed during the outburst. The paper is organized in the following way. In Section 2, we describe the observations and process of data analysis. In Section 3, we present the timing and spectral analysis results. In Section 4, we discuss our findings and finally, in Section 5, we summarize our results.

## 2 OBSERVATION AND DATA REDUCTION

### *NuSTAR*

The transient BHC MAXI J1813–095 was observed with *NuSTAR* at three epochs during the declining phase of the 2018 outburst (see Table 1). *NuSTAR* (Harrison et al. 2013) is the first hard X-ray focusing observatory launched by NASA. It consists of two identical focusing modules: FPMA and FPMB. These modules are sensitive to X-ray photons in the range of 3 – 79 keV. We reprocessed data from the *NuSTAR* observations with the help of *NuSTAR* data analysis software (*nustardas*, version 1.4.1<sup>1</sup>). Cleaned event files were produced and calibrated applying standard filtering criteria with the *nupipeline* task by using the latest calibration files<sup>2</sup>. We chose circular regions with radii 120 arcsec centered at the source coordinates for the source and away from the source for the background products. The *nuproduct* task was employed to extract source and background spectra. We re-binned the source spectra to 20 counts per bin with the *grppha*<sup>3</sup> task.

### *Swift*

*Swift* observed MAXI J1813–095 at two epochs simultaneously with two *NuSTAR* observations. In total, *Swift* observed MAXI J1813–095 twelve times between 2018 February 20 and 2018 March 25. All the observations were carried out with the *Swift*/XRT in the energy range of 0.5–10 keV. *Swift*/XRT observations of MAXI J1813–095 were carried out in windowed-timing (WT) mode except the first observation which was in photon-counting (PC) mode. We extracted cleaned event files with the *FTOOLS*

<sup>1</sup> <https://heasarc.gsfc.nasa.gov/docs/nustar/analysis/>

<sup>2</sup> <http://heasarc.gsfc.nasa.gov/FTP/caldb/data/nustar/fpm/>

<sup>3</sup> <https://heasarc.gsfc.nasa.gov/ftools/caldb/help/grppha.txt>

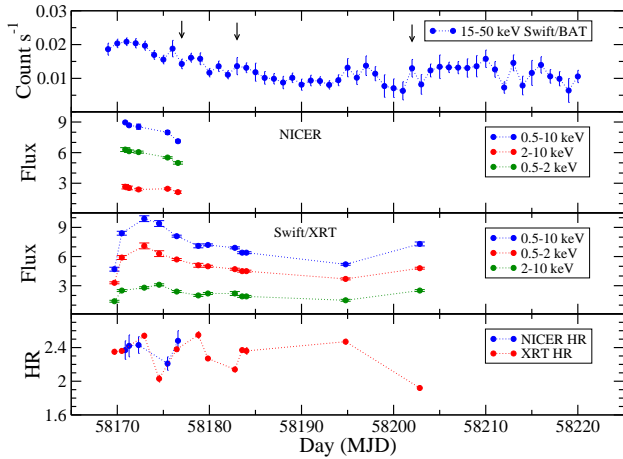


**Fig. 1** The top panel features the 15 – 50 keV *Swift*/BAT light curve of MAXI J1813–095 from 2018 February 16 (MJD 58165) to 2018 April 17 (MJD 58225). The arrows represent the epochs of the *NuSTAR* observation of the source. In the second panel, absorption corrected flux in 0.5 – 10 keV, 0.5 – 2 keV and 2 – 10 keV energy ranges, obtained from *NICER* observations, are shown. The third panel displays the variation of 0.5 – 10 keV, 0.5 – 2 keV and 2 – 10 keV *Swift*/XRT unabsorbed flux during the outburst. The fluxes are plotted in the unit of  $10^{-10}$  erg  $\text{cm}^{-2}$   $\text{s}^{-1}$ . In the bottom panel, the HR, i.e., ratio between fluxes in 2 – 10 keV and 0.5 – 2 keV ranges, obtained from *NICER* and XRT data, are shown.

task `xrtpipeline`<sup>4</sup>. We chose a circular region with radius 30 arcsec for source and background products. Light curves, source and background spectra were extracted by utilizing `XSELECT` v2.4<sup>5</sup>.

## NICER

MAXI J1813–095 was also observed with *NICER* at several epochs during the 2018 X-ray outburst. *NICER* is an X-ray timing instrument (XTI; Gendreau et al. 2012) that was attached to the International Space Station in June 2017. It is sensitive to soft X-ray photons in the 0.2 – 12 keV range. The XTI consists of 56 X-ray concentrating optics, each attached to a silicon drift detector (Prigozhin et al. 2012). There are only 52 detector units that are active, providing a total effective area of  $1900 \text{ cm}^2$  at 1.5 keV. Unprecedented timing and spectral sensitivities of  $\sim 100$  ns (root mean square, rms) and  $\sim 85$  eV at 1 keV can also be achieved by *NICER*, respectively. For the study of outburst evolution of MAXI J1813–095, we relied on publicly available data from *NICER* monitoring between 2018 February 21 and February 27. The total effective exposure of

**Table 1** Log of *NICER*, *NuSTAR* and *Swift* Observations of the Transient BHC MAXI J1813–095

ID	Date of Obs. (yyyy-mm-dd)	Obs. ID	Exp (ks)
<i>NICER</i>			
X1	2018–02–21	1200090101	0.6
X2	2018–02–22	1200090102	0.4
X3	2018–02–23	1200090103	2.4
X4	2018–02–26	1200090104	1.1
X5	2018–02–27	1200090105	1.3
<i>NuSTAR</i>			
N1	2018–02–28	80402303002	23.2
N2	2018–03–06	80402303004	20.5
N3	2018–03–25	80402303006	20.4
<i>Swift</i> /XRT			
S1	2018–03–06	00088654002	1.8
S2	2018–03–25	00088654004	1.9

these observations with observation ids 1200090101–1200090105 is about 5.5 ks. For analysis, the data were first reprocessed with the ‘`nicerl2`’<sup>6</sup> script in the presence of the latest updated calibration files of version 20200722. Standard GTI was also generated using the ‘`nimaketime`’ task. The cleaned events obtained after the reprocessing were then utilized for extracting the light curve and spectrum in the `FTOOLS` `XSELECT` environment. For spectral analysis, ancillary response file and response matrix file of version 20200722 are considered in our analysis. The background corresponding to each observation id is simulated by employing the `nibackgen3C50`<sup>7</sup> tool (Remillard et al, in prep.).

## 3 RESULT

### 3.1 Timing Analysis

BHC MAXI J1813–095 was first detected on 2018 February 19 while undergoing the recent X-ray outburst. The outburst lasted for about  $\sim 50$  d. The evolution of the outburst is shown in Figure 1 using data from *Swift*/BAT monitoring, *NICER* and *Swift*/XRT observations. In the top panel of Figure 1, we show the outburst profile of the source with the *Swift*/BAT monitoring light curve in the 15 – 50 keV energy range. It can be seen that the outburst peaked on 2018 February 22 (MJD 58171) with intensity  $\sim 95$  mCrab in the 15 – 50 keV range. The outburst was followed with *NICER* from 2018 February 21 (MJD 58170.86), when the source was at its peak with a source count rate of  $157 \pm 0.5$  count  $\text{s}^{-1}$  in the 0.5 – 10 keV energy range. The second panel of the figure

<sup>4</sup> <https://www.swift.ac.uk/analysis/xrt/>

<sup>5</sup> <https://www.swift.ac.uk/analysis/xrt/xselect.php>

<sup>6</sup> [https://heasarc.gsfc.nasa.gov/docs/nicer/analysis\\_threads/nicerl2/](https://heasarc.gsfc.nasa.gov/docs/nicer/analysis_threads/nicerl2/)

<sup>7</sup> [https://heasarc.gsfc.nasa.gov/docs/nicer/tools/nicer\\_bkg\\_est\\_tools.html](https://heasarc.gsfc.nasa.gov/docs/nicer/tools/nicer_bkg_est_tools.html)

**Table 2** Spectral Fitting Parameters Obtained from the *NICER* Observations

ID	$T_{\text{in}}$ (keV)	DBB Norm.	$\Gamma$	Flux	$\chi^2/\text{dof}$
X1	$0.57 \pm 0.06$	$43.8 \pm 2.1$	$1.53 \pm 0.05$	$8.96 \pm 0.12$	552/580
X2	$0.56 \pm 0.05$	$56.1 \pm 2.4$	$1.52 \pm 0.06$	$8.68 \pm 0.11$	569/537
X3	$0.54 \pm 0.03$	$40.5 \pm 2.0$	$1.54 \pm 0.03$	$8.54 \pm 0.15$	797/750
X4	$0.58 \pm 0.09$	$16.1 \pm 1.2$	$1.55 \pm 0.04$	$8.22 \pm 0.19$	592/628
X5	$0.61 \pm 0.05$	$18.8 \pm 1.2$	$1.52 \pm 0.04$	$8.12 \pm 0.15$	672/665

$N_{\text{H}}$  was fixed at  $1.1 \times 10^{-22} \text{ cm}^{-2}$ . Errors are quoted with 90% confidence;  
Flux is in the unit of  $10^{-10} \text{ erg cm}^{-2} \text{ s}^{-1}$  and estimated in the 0.5 – 10 keV energy range.

displays the light curve of the source in the 0.5 – 10, 0.5 – 2 keV and 2 – 10 keV energy ranges, obtained from *NICER* observations. The third panel of the figure represents absorption corrected source flux in 0.5 – 2 keV, 2 – 10 keV and 0.5 – 10 keV ranges, estimated from *Swift*/XRT data. From Figure 1 (second panel), it can be seen that the *NICER* observations started when the source was brightest (on 2018 February 21, MJD 58170.86). However, the *Swift*/XRT flux, as featured in the third panel, was maximum on 2018 February 23 (MJD 58172.93). It should be noted that the data presented in the second and third panels are in the 0.5 – 10 keV range. The difference in the outburst peaking times in *NICER* and *Swift*/XRT data was due to the fact that the source was not observed with the *Swift*/XRT between MJD 58170.69 and MJD 58172.93 (between 2018 February 21 and 2018 February 23). The actual peak of the outburst might have been missed in the *Swift*/XRT observation. In the bottom panel of Figure 1, the hardness ratio (HR) (ratio between fluxes in 2 – 10 keV and 0.5 – 2 keV ranges) of the source during the outburst is plotted by using *NICER* and *Swift*/XRT data. It can be seen from the figure that the source intensity gradually decreased from 2018 February 21 as the outburst entered its declining phase. A brief re-brightening was observed on 2018 March 25. Soon after that, the source entered its quiescent state. To investigate the spectral evolution of the source during the outburst, we plotted the hardness-intensity diagram (HID) (source flux vs. HR), obtained from the *Swift*/XRT and *NICER* observations in the 0.5 – 10 keV energy range and depicted in Figure 2. The rising (increasing flux) and declining (decreasing flux) phase of the outburst can be traced in the HID (Fig. 2) through the *Swift*/XRT data points. It can be seen that the data points in the HID appear to lie in the branch corresponding to the hard state of the “Q-diagram” of BH sources (Homan & Belloni 2005). The X-ray intensity varied during the outburst, though the HR remained approximately the same, indicating no change in spectral states. Considering the evolution of 0.5 – 2 keV and 2 – 10 keV *Swift*/XRT light curves and the HR plot (Fig. 1) and the HID (Fig. 2), it is clear that the

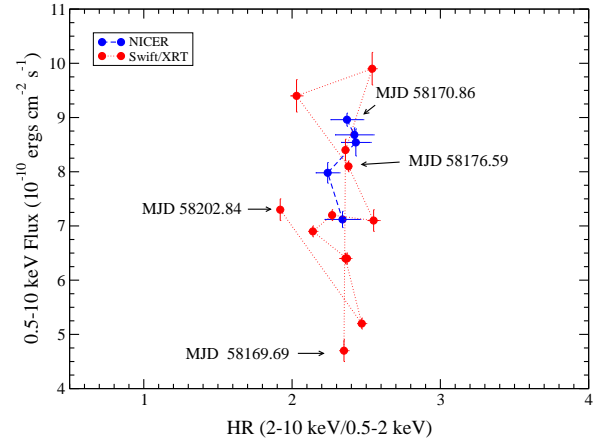


**Fig. 2** HID is displayed for 0.5 – 10 keV *Swift*/XRT and *NICER* observations. Red and blue points represent *Swift* and *NICER* observations, respectively. Hardness ratio is defined as the ratio between 2 – 10 keV flux and 0.5 – 2 keV flux. The 0.5 – 10 keV flux is in the unit of  $10^{-10} \text{ erg cm}^{-2} \text{ s}^{-1}$ .

source remained in the hard spectral state during the entire outburst in 2018.

We analyzed the 0.01 s light curves in the 0.5 – 10 keV range obtained from *NICER* observations. White-noise subtracted PDSs were generated by applying the fast Fourier transformation (FFT) technique on the light curves with the FTOOLS task `powspec norm=-2` for different intervals such as 2048, 4096 and 8192. In Figure 3, we display the PDSs generated from the 0.01 s light curves from the *NICER* observations on (a) 2018 February 21 (Obs ID: 1200090101), (b) 2018 February 23 (Obs ID: 1200090103) and (c) 2018 February 27 (1200090105). The 0.01 s binning time allowed us to search for presence/absence of QPOs up to 50 Hz in each PDS. However, we did not find any signature of the presence of QPO in the PDS of any of the observations. All the PDSs exhibited weak red-noise with flat top noise up to 0.1 Hz. A strong rms is observed in all the PDSs with  $\text{rms} \simeq 20\% - 30\%$  in the 0.1–50 Hz band. We also investigated the presence of QPOs in the PDS obtained from the *Swift*/XRT light curves, and obtained similar results. We attempted to search for the signature of high frequency QPOs by

generating PDSs from light curves with 0.004 s time bin from *NICER* observations. However, as in the case of searching for low frequency QPOs, there was no signature of the presence of any high frequency QPOs in the PDSs up to 1250 Hz.

### 3.2 Spectral Analysis

We study the BHC MAXI J1813–095 during its 2018 outburst using data from *Swift*/XRT, *NICER* and *NuSTAR* observations in the energy range of 0.5 – 78 keV. We carry out spectral analysis with HEASARC’s spectral analysis software package XSPEC v12.10<sup>8</sup> (Arnaud 1996). For interstellar absorption, we relied on the TBabs model with Wilms abundances (Wilms et al. 2000).

#### 3.2.1 *Swift*

MAXI J1813–095 was observed with the *Swift* observatory at twelve epochs during the 2018 X-ray outburst. The source and background spectra, effective area and response files were generated as described in the previous section, and incorporated in the spectral fitting. The 0.5 – 10 keV XRT spectra were fitted well with an absorbed power law model. We fixed the hydrogen column density ( $N_{\text{H}}$ ) at  $1.1 \times 10^{22} \text{ cm}^{-2}$  (Armas Padilla et al. 2019). The power-law photon index ( $\Gamma$ ) was found to vary between 1.54 and 1.68 during the outburst period. We also calculated the unabsorbed flux in the 0.5 – 2 keV and 2 – 10 keV energy bands utilizing the ‘cflux’ command in XSPEC. In Figure 4(a) (left panel), we feature a representative 0.5 – 10 keV *Swift*/XRT spectrum fitted with a powerlaw model, observed on 2018 February 25 (Obs ID : 00010563004).

#### 3.2.2 *NICER*

*NICER* observed MAXI J1813–095 five times during the 2018 outburst. The 0.5 – 10.0 keV spectra were fitted with the absorbed power law (powerlaw) model along with the disk-blackbody (diskbb) component. Spectra from all the observations were fitted well with this model. The inner disk temperature ( $T_{\text{in}}$ ) varied between 0.54 – 0.61 keV along with an approximately constant power-law photon index ( $\Gamma$ ) ( $\sim 1.52 - 1.55$ ). No signature of the Fe  $K\alpha$  line was observed in the *NICER* data. We display a representative 0.5–10 keV *NICER* spectrum in Figure 4(b) (middle panel), observed on 2019 February 22 (Obs ID:

1200090102). The powerlaw + diskbb model fitted spectral parameters are listed in Table 2.

#### 3.2.3 *Swift* + *NuSTAR*

*NuSTAR* observed MAXI J1813–095 three times during the 2018 X-ray outburst. Among those, two observations were made simultaneously with the *Swift*/XRT. We attempted to carry out simultaneous spectral fitting of *Swift*/XRT and *NuSTAR* data with an absorbed power law model. However, fitting the broadband spectra with the absorbed power law model did not provide us satisfactory fitting with  $\chi^2 = 1470$  for 1122 degrees of freedom (dof) for the *NuSTAR* observation on 2018 February 28 (N1 in Table 1). Signatures of a disk and Fe  $K\alpha$  emission line were seen in the residuals. Adding a diskbb component to the model improves the fit with  $\chi^2 = 1328$  for 1120 dof. We further added a Gaussian function for the Fe  $K\alpha$  line, which significantly improved the fit with  $\chi^2 = 1155$  for 1117 dof. The other two *NuSTAR* observations (N2 and N3 in Table 1) when fitted along with simultaneous *Swift*/XRT data (S1 and S2 in Table 1), also showed similar results. Therefore, the TBabs\*(diskbb+powerlaw+Gaussian) model fits well the broadband spectra of MAXI J1813–095 from *NuSTAR* and *Swift*/XRT observations. The power-law photon index ( $\Gamma$ ) was found to be 1.56, 1.57 and 1.62 for N1, N2+S1 and N3+S2, respectively. The inner disk temperature ( $T_{\text{in}}$ ) varied between 0.61 keV and 0.57 keV. It was found that during all three *NuSTAR* observations, the power-law flux dominated over the thermal flux. The fraction of thermal flux was less than  $\sim 10\%$  of total flux in the 0.5 – 78 keV range, obtained from simultaneous fitting *Swift*/XRT and *NuSTAR* data, and less than 1% of total flux in the 3 – 78 keV energy range obtained from fitting *NuSTAR* data (N1). The best-fit model parameters are expressed in Table 3.

We often observed a reflection hump at around  $\sim 15 - 30$  keV in the hard state spectra (George & Fabian 1991; Matt et al. 1991). Often, the presence of reflection makes the spectra harder. Unusually, hard spectra are observed in MAXI J1813–095 with low photon index. In order to probe the spectral nature and reflection continuum further, we explore the ‘reflection’ with convolution model for reflection reflect (Magdziarz & Zdziarski 1995). This model describes the reflection from relatively cold neutral material. We fixed heavy element abundances and iron abundances at the solar value (i.e. 1). We allowed the relative reflection ( $R_{\text{refl}}$ ), photon index ( $\Gamma$ ) and inclination angle of the system (as  $\cos \text{incl}$ ) to vary. All three observations yielded a marginally improved fit compared

<sup>8</sup> <https://heasarc.gsfc.nasa.gov/docs/xanadu/xspec/>

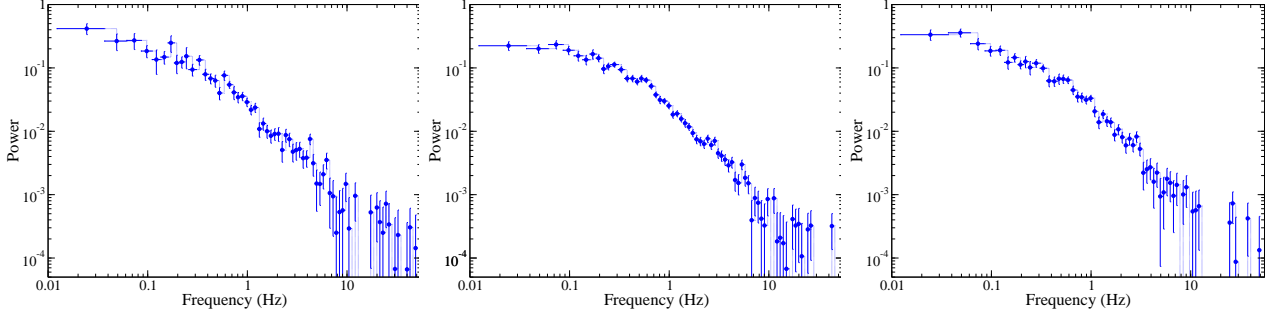


**Fig. 3** The PDSs obtained from the *NICER* observations of MAXI J1813–095 on 2018 February 21 (Obs. ID: 1200090101, *left panel*), 2018 February 23 (Obs. ID: 1200090103, *middle panel*) and 2018 February 27 (Obs. ID: 1200090105, *right panel*). The PDSs are generated from 0.01 s light curves in the 0.5 – 10 keV energy range.

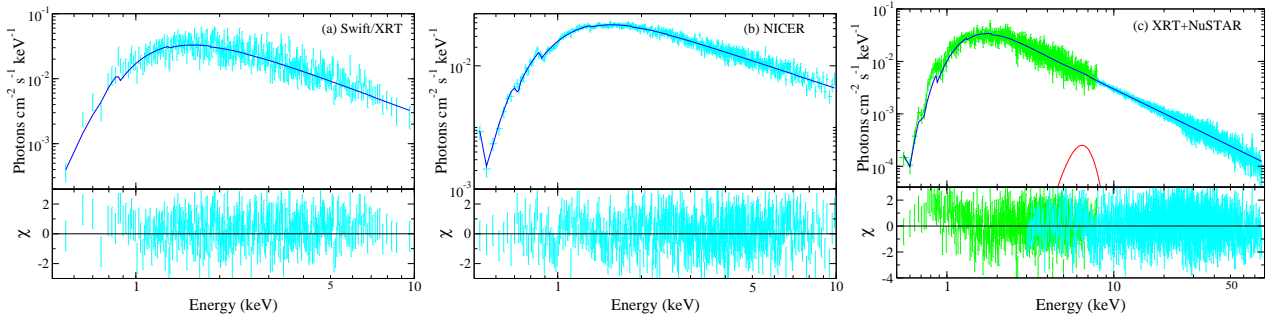


**Fig. 4** Spectra of BHC MAXI J1813–095 along with the best-fit model and residuals obtained from the (a) *Swift*/XRT observation on 2018 February 25 (Obs ID: 00010563004) in the 0.5 – 10 keV range (*left panel*), (b) *NICER* observation on 2018 February 22 (Obs ID: 1200090102) in the 0.5 – 10 keV range (*middle panel*) and (c) *Swift*/XRT and *NuSTAR* simultaneous observations on 2018 March 6 (*Swift* Obs ID: 00088654002; *NuSTAR* Obs ID: 80402303004) in the 0.5 – 78 keV range (*right panel*) are displayed. The 0.5 – 10 keV *Swift*/XRT (*left panel*), 0.5 – 10 keV *NICER* (*middle panel*) and 0.5 – 78 keV *Swift*/XRT+*NuSTAR* (*right panel*) spectra were fitted with the TBabs\*powerlaw, TBabs\*(diskbb+powerlaw) and TBabs (diskbb+powerlaw+Gaussian) models, respectively. The residuals obtained from the spectral fitting are depicted in the bottom panels.

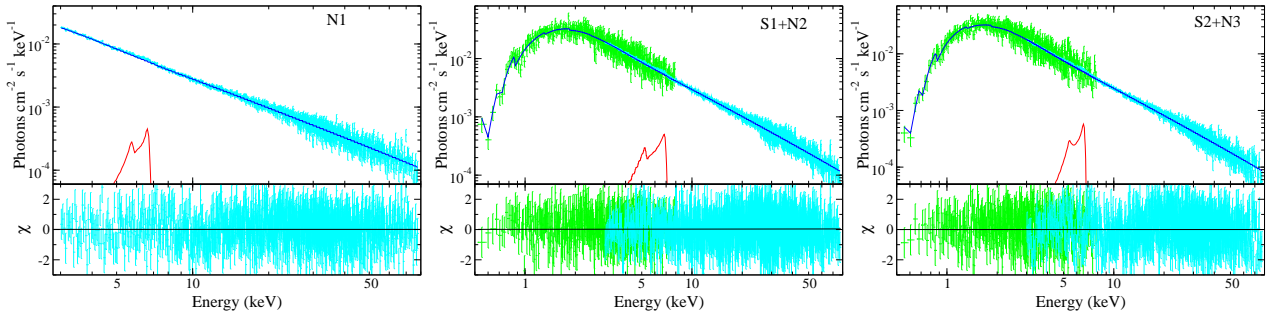


**Fig. 5** The 3 – 78 keV (*left panel*) and 0.5 – 78 keV (*middle and right panels*) TCAF+LAOR model fitted spectra and residuals are displayed for the first *NuSTAR* (N1) and *NuSTAR*+*Swift*/XRT (N2+S1 and N3+S2) observations, respectively.

to the powerlaw model fitting. The photon index  $\Gamma$  was constant at around 1.65. The  $R_{\text{refl}}$  was 0.15, 0.22 and 0.25 for N1, N2+S1, and N3+S2, respectively. The  $\cos(\text{incl})$  varied between 0.71 and 0.88, which transformed the inclination angle between  $28^\circ$  and  $45^\circ$ . The inner disk temperature ( $T_{\text{in}}$ ) was observed to be 0.56, 0.48 and 0.40 keV for N1, N2+S1 and N3+S2, respectively.

Next, we used physical model TCAF as a local additive model in XSPEC (Debnath et al. 2014, 2015).

Along with the TCAF, we utilized the LAOR model (Laor 1991) to incorporate the iron  $K\alpha$  emission line. The TCAF model has five input parameters: the mass of the BH ( $M_{\text{BH}}$ ) in solar mass ( $M_\odot$ ), the Keplerian disk accretion rate ( $\dot{m}_d$ ) in Eddington rate ( $\dot{M}_{\text{Edd}}$ ), the sub-Keplerian halo accretion rate ( $\dot{m}_h$ ) in Eddington rate ( $\dot{M}_{\text{Edd}}$ ), the shock location or the size of the Compton cloud ( $X_s$ ) in Schwarzschild radius ( $r_s$ ) and the shock compression ratio ( $R$ , ratio between post-shock matter density and

**Table 3** Best-fit spectral parameters obtained from *NuSTAR* and *Swift*/XRT observations

Model Comp.	Parameter	<i>NuSTAR</i> + <i>Swift</i> /XRT		
		<i>NuSTAR</i> N1	N2+S1	N3+S2
diskbb	$T_{\text{in}}$ (keV)	$0.62^{+0.07}_{-0.05}$	$0.61^{+0.04}_{-0.10}$	$0.57^{+0.05}_{-0.08}$
	norm	$92.6^{+8.4}_{-7.9}$	$103.6^{+12.9}_{-14.2}$	$121.0^{+15.5}_{-12.8}$
Powerlaw	$\Gamma$	$1.56^{+0.05}_{-0.04}$	$1.57^{+0.05}_{-0.05}$	$1.62^{+0.04}_{-0.08}$
	norm	$0.15^{+0.03}_{-0.03}$	$0.11^{+0.02}_{-0.03}$	$0.10^{+0.01}_{-0.01}$
Gaussian	LE (keV)	$6.20^{+0.25}_{-0.22}$	$6.47^{+0.27}_{-0.24}$	$6.23^{+0.19}_{-0.28}$
	$\sigma$ (keV)	$0.77^{+0.06}_{-0.09}$	$0.97^{+0.10}_{-0.07}$	$0.86^{+0.06}_{-0.09}$
	norm*	$9.47^{+0.24}_{-0.29}$	$3.77^{+0.29}_{-0.22}$	$7.21^{+0.33}_{-0.21}$
	$\chi^2/\text{dof}$	1155/1117	1610/1555	1699/1558
diskbb	$T_{\text{in}}$ (keV)	$0.56^{+0.05}_{-0.08}$	$0.48^{+0.04}_{-0.06}$	$0.40^{+0.06}_{-0.10}$
	norm	$66.5^{+2.9}_{-4.4}$	$138.7^{+5.1}_{-7.9}$	$145.6^{+6.5}_{-8.8}$
Powerlaw	$\Gamma$	$1.64^{+0.04}_{-0.08}$	$1.66^{+0.03}_{-0.07}$	$1.65^{+0.05}_{-0.06}$
	norm	$0.12^{+0.01}_{-0.01}$	$0.13^{+0.02}_{-0.03}$	$0.13^{+0.02}_{-0.02}$
Reflect	$R_{\text{refl}}$	$0.15^{+0.02}_{-0.03}$	$0.22^{+0.03}_{-0.04}$	$0.25^{+0.02}_{-0.04}$
	$\cos(\text{incl})$	$0.88^{+0.02}_{-0.04}$	$0.71^{+0.05}_{-0.06}$	$0.85^{+0.03}_{-0.07}$
Gaussian	LE (keV)	$6.20^{+0.18}_{-0.22}$	$6.56^{+0.07}_{-0.20}$	$6.33^{+0.016}_{-0.23}$
	$\sigma$ (keV)	$0.78^{+0.20}_{-0.13}$	$0.97^{+0.12}_{-0.14}$	$0.81^{+0.12}_{-0.15}$
	norm*	$2.51^{+0.25}_{-0.17}$	$2.06^{+0.26}_{-0.28}$	$1.28^{+0.20}_{-0.24}$
	$\chi^2/\text{dof}$	1126/1115	1555/1553	1589/1556
TCAF	$M_{\text{BH}}$ ( $M_{\odot}$ )	$7.38^{+1.43}_{-1.46}$	$7.44^{+1.24}_{-1.56}$	$7.40^{+1.33}_{-1.33}$
	$\dot{m}_{\text{d}}$ ( $\dot{M}_{\text{Edd}}$ )	$0.07^{+0.01}_{-0.01}$	$0.05^{+0.01}_{-0.01}$	$0.06^{+0.01}_{-0.02}$
	$\dot{m}_{\text{h}}$ ( $\dot{M}_{\text{Edd}}$ )	$0.54^{+0.03}_{-0.04}$	$0.51^{+0.02}_{-0.05}$	$0.52^{+0.04}_{-0.06}$
	$X_{\text{s}}$ ( $r_{\text{s}}$ )	$93^{+9}_{-11}$	$111^{+10}_{-14}$	$113^{+9}_{-11}$
	$R$	$2.80^{+0.15}_{-0.16}$	$2.82^{+0.10}_{-0.18}$	$2.79^{+0.12}_{-0.16}$
	$N_{\text{tcaf}}$	$1.62^{+0.08}_{-0.11}$	$1.65^{+0.07}_{-0.12}$	$1.67^{+0.09}_{-0.12}$
LAOR	LE (keV)	$6.45^{+0.22}_{-0.16}$	$6.59^{+0.16}_{-0.23}$	$6.43^{+0.16}_{-0.20}$
	index	$1.75^{+0.03}_{-0.04}$	$1.89^{+0.06}_{-0.07}$	$1.87^{+0.06}_{-0.09}$
	$R_{\text{in}}$ ( $r_{\text{g}}$ )	$2.64^{+0.10}_{-0.06}$	$2.59^{+0.11}_{-0.08}$	$2.58^{+0.11}_{-0.08}$
	$R_{\text{out}}$ ( $r_{\text{g}}$ )	$68.1^{+3.1}_{-5.5}$	$60.2^{+5.2}_{-6.5}$	$75.6^{+2.5}_{-3.6}$
	$\theta_{\text{incl}}$ (deg)	$35.08^{+1.42}_{-2.77}$	$36.26^{+1.48}_{-2.65}$	$31.88^{+1.65}_{-2.23}$
	norm*	$5.33^{+0.41}_{-0.37}$	$8.02^{+0.38}_{-0.45}$	$7.07^{+0.32}_{-0.46}$
$\chi^2/\text{dof}$	1129/1110	1583/1555	1595/1556	
$F_{0.1-100}^a$	0.1 – 100 keV	$2.44^{+0.15}_{-0.11}$	$1.86^{+0.09}_{-0.12}$	$1.94^{+0.12}_{-0.10}$
$f_{\text{th}}^b$	0.5 – 78 keV	—	5.4%	10%
	3 – 78 keV	0.8%	0.7%	0.9%

\*: in the unit of  $10^{-4}$  ph cm $^{-2}$  s $^{-1}$ ;  $a$ : in the unit of  $10^{-8}$  erg s $^{-1}$  cm $^{-2}$ ;  $b$  Thermal fraction, defined as  $F_{\text{d}}/(F_{\text{d}} + F_{\text{PL}})$ . All errors are quoted at the 90% confidence level.

pre-shock matter density). Along with these, we obtain normalization ( $N$ ), which is a function of mass of the BH, the distance of the source and inclination angle of the system. As these three parameters are intrinsic to the system, the normalization parameter  $N$  should remain unchanged during the outburst (Jana et al. 2017, 2020a). The TCAF+LAOR model gave us a good fit for all three observations. The TCAF model fitted spectra are shown in Figure 5. We display the Fe  $K\alpha$  line intensity in Figure 6.

While fitting the data with the TCAF model, we kept mass of the BH as a free parameter. We obtained  $M_{\text{BH}}$  as 7.38, 7.44 and 7.40  $M_{\odot}$  from N1, N2+S1 and N3+S2, respectively. The Keplerian disk mass accretion rate  $\dot{m}_{\text{d}}$  varied between 0.07  $\dot{M}_{\text{Edd}}$  and 0.05  $\dot{M}_{\text{Edd}}$ . The sub-Keplerian halo accretion rate  $\dot{m}_{\text{h}}$  varied between 0.54  $\dot{M}_{\text{Edd}}$  and 0.52  $\dot{M}_{\text{Edd}}$ . The dominance of the sub-

Keplerian flow indicates the hard spectral state of the source during the observation period. We also observed that the shock moved outward from 93  $r_{\text{s}}$  to 113  $r_{\text{s}}$ . Thus, the size of the Compton cloud increased as the outburst progressed. The shock was strong during all three observations with the shock compression ratio  $R \sim 2.80$ . During all three observations, the normalization was roughly constant with  $N \sim 1.65$ . The TCAF model fitted results are provided in Table 3. We used the LAOR model along with the TCAF for a relativistic broad iron line. The broad Fe  $K\alpha$  line is depicted in Figure 6.

#### 4 DISCUSSION

We studied MAXI J1813–095 during its 2018 outburst using data from *Swift*/XRT, *NICER* and *NuSTAR* observatories in the energy range of 0.5 – 78 keV. *Swift*/XRT

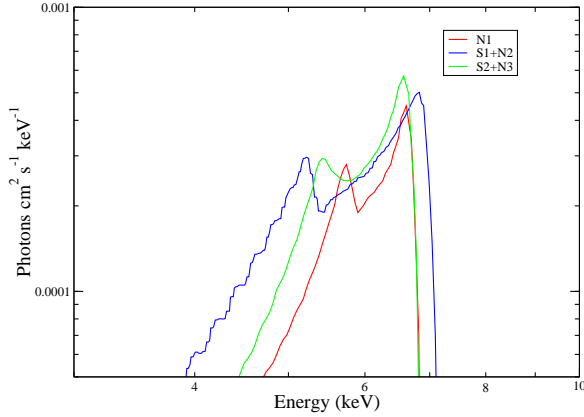


**Fig. 6** The Fe  $K\alpha$  line intensity is shown for three *NuSTAR* observations.

observed the source twelve times during the outburst. The 0.5 – 10 keV *Swift*/XRT data were fitted with an absorbed power law model. The disk component was not required while fitting the spectra with the absorbed power law model. We also did not find any evidence of the Fe  $K\alpha$  line in the 0.5 – 10 keV *Swift*/XRT data. *NICER* observed MAXI J1813–095 at five epochs during the outburst. In contrast to the 0.5 – 10 keV *Swift*/XRT spectra, the 0.5 – 10 keV *NICER* spectra required a disk component along with the power law continuum. Superior spectral resolution of *NICER* over *Swift*/XRT enabled detection of an additional spectral component, which *Swift*/XRT could not detect.

Interestingly, when we examined the 3 – 78 keV *NuSTAR* (N1) spectra or the 0.5 – 78 keV *Swift*/XRT+*NuSTAR* (N2+S1 and N3+S2) spectra, a disk component, an Fe  $K\alpha$  emission line and reflection components were required along with the power law continuum. This suggests that the 0.5 – 10 keV *Swift*/XRT or *NICER* spectra did not provide complete information on the source spectra. Moreover, the exposure time of each *NuSTAR* observation is long (on average  $\sim 20$  ks), while the *NICER* and *Swift*/XRT observations have short exposure times ( $\sim 1 - 2$  ks, see Table 1). Thus, the long exposure of *NuSTAR* and its broadband coverage helped to detect additional spectral features in the source.

#### 4.1 Outburst Profile

The 2018 outburst of MAXI J1813–095 continued for  $\sim 50$  d. The peak luminosity of the source was observed on 2018 February 23, with  $L_{\text{peak}} = 4.25 \times 10^{36} (d/6)^2 \text{ erg s}^{-1}$  in the 0.5 – 10 keV energy band. However, one needs to calculate the luminosity in a broad energy range to extract detailed information. We calculated bolometric luminosity of the source for three *NuSTAR* observations

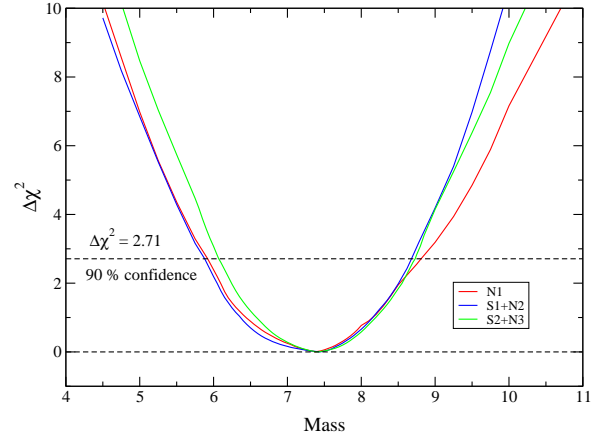


**Fig. 7** The variation of  $\Delta\chi^2$  is demonstrated with the mass of the BH ( $M_{\text{BH}}$ ) for three *NuSTAR* observations.

from unabsorbed flux in the 0.1 – 100 keV energy band. The bolometric luminosity of the source was estimated to be  $L = 7.9 - 10.5 \times 10^{37} (d/6)^2 \text{ erg s}^{-1}$ . Thus,  $L/L_{\text{Edd}} \sim 0.06 - 0.07$ , for a BH with mass  $7.4 M_{\odot}$ . Since the observed mass accretion rate is  $\sim 0.6 \dot{M}_{\text{Edd}}$ , the accretion efficiency is very low during the 2018 outburst.

During the entire outburst, the hard X-ray photons (2 – 10 keV range) dominate over the soft X-ray photons in the 0.5 – 2 keV range (see Fig. 1). High HR was also observed during the outburst. We estimated thermal flux ( $F_{\text{d}}$ ) and non-thermal flux ( $F_{\text{PL}}$ ) from the `diskbb` and `powerlaw` model components, respectively, from the combined *Swift*/XRT and *NuSTAR* simultaneous spectral fitting in the 0.5 – 78 keV range. We find that the fraction of thermal flux with respect to non-thermal flux ( $f_{\text{th}} = F_{\text{d}}/F_{\text{PL}}$ ) is less than 10% in the 0.5 – 78 keV range and less than 1% in the 3 – 78 keV energy range. The spectral analysis results (low  $\Gamma$ , high sub-Keplerian flow rate over the Keplerian flow rate, strong shock, etc.) indicate that the source was in the hard state during the *NuSTAR* observations. Thus, together with the spectral properties, the evolution of 0.5 – 2 keV and 2 – 10 keV fluxes, high HR and HID, we infer that the source remained in the hard state during the entire outburst. Strong variabilities ( $> 20\% - 30\%$  rms) observed in the PDSs also support this.

The 2018 outburst of MAXI J1813–095 can be considered as a ‘failed’ outburst as the source failed to make the state transition to softer spectral states. The observed HID of the source is similar to the HID of other sources during respective ‘failed’ outbursts, where the HRs do not change despite the change in X-ray intensity (Tetarenko et al. 2016). In a detailed study of 132 outbursts, Tetarenko et al. (2016) reported that the mean outburst duration for ‘failed’ outbursts is about  $\sim 290$

d. However, many ‘failed’ outbursts were observed to be as short as the 2018 outburst of MAXI J1813–095. For example, the outburst duration of the 1998 outburst of XTE J0421+560 (Belloni et al. 1999) and 2011 outburst of Swift J1357.2–0933 (Armas Padilla et al. 2013) are 49 d and 76 d, respectively. In general, failed outbursts are ‘faint’ with peak luminosity  $L_{\text{peak}} \lesssim 10^{36} \text{ erg s}^{-1}$  (e.g. the 2000 outburst of XTE J1118+480 (Chatterjee et al. 2019), the 2003 outburst of XTE J1550–564 (Sturmer & Shrader 2005)), whereas the peak luminosity during complete outbursts,  $L_{\text{peak}} \sim 10^{38} \text{ erg s}^{-1}$  e.g. the 2009 outburst of XTE J1752–223 (Reis et al. 2011), the 2017 outburst of MAXI J1535–571 (Stiele & Kong 2018), the 2019 outburst of MAXI J1348–630 (Jana et al. 2020b) and the 2019–2020 outburst of MAXI J0637–430 (Jana et al. 2021). The peak luminosity of MAXI J1813–095 during the present outburst is  $L_{\text{peak}} \sim 10^{36} \text{ erg s}^{-1}$ , which is consistent with other ‘failed’ outbursts. Thus, MAXI J1813–095 joined the ever-increasing list of ‘failed’ outbursts (e.g. the 2008 outburst of H 1743–322 (Capitanio et al. 2009), the 2011 and 2012 outbursts of MAXI J1836–194 (Jana et al. 2016, 2020a), the 2017 outburst of Swift J1357.2–0933 (Mondal & Chakrabarti 2019) and the 2017 outburst of GX 339–4 (García et al. 2019).)

## 4.2 Accretion Geometry

In general, an outburst is triggered when the viscosity is suddenly enhanced at the outer edge of the disk (Ebisawa et al. 1996). The accreting matter loses angular momentum when the viscosity rises and rushes towards the BH. The low viscosity sub-Keplerian flow moves inward roughly on the free-fall time scale, whereas the Keplerian disk moves inward on the viscous time scale. If the viscosity is sufficiently high, the Keplerian disk moves closer to the BH and cools the CENBOL and the source undergoes state transition (Giri & Chakrabarti 2012; Mondal et al. 2017). However, if the viscosity does not rise high enough, the Keplerian disk remains at a large distance from the BH. Hence, the Keplerian disk cannot cool the CENBOL efficiently. As a result, the source does not enter the softer spectral states. In the 2018 outburst of MAXI J1813–095, it appears that the viscosity did not become high enough, and the source did not enter in the softer spectral states. Although the Keplerian disk accretion rate was low, the continuous supply of sub-Keplerian matter leads to increase of high energy flux, as well as the total flux, which leads to higher HR when the flux was high. This is not observed in a regular outburst. The source entered the declining phase of the outburst when the viscosity is turned off. The shock moved outward

as the accretion rates were decreased and the source entered the quiescent state.

We did not observe any QPO in the PDS of the source. It is understood that the oscillation of the CENBOL or the Compton cloud produces the QPOs (Molteni et al. 1996; Giri & Chakrabarti 2012). Sharp QPOs are produced when a strong shock oscillates and the resonance condition is satisfied (Molteni et al. 1996; Chakrabarti et al. 2015). The resonance condition is satisfied when the cooling time of the post-shock matter matches the infall time. On the other hand, a weak QPO is produced due to the non-satisfaction of the Rankine-Hugoniot condition or oscillation of the shock-less barrier or weak shock oscillation (Ryu et al. 1997). A strong shock was formed during the 2018 outburst of MAXI J1813–095. However, due to the low Keplerian disk accretion rate, and high sub-Keplerian halo rate, the cooling was inefficient. Thus, it is plausible that non-satisfaction of the resonance condition is behind non-observation of QPOs. This is already reported in several sources that non-satisfaction of resonance condition is the reason behind non-observation of QPOs (Chakrabarti et al. 2015; Jana et al. 2020a,b).

In the first two *NuSTAR* observations (N1 and N2), the source was observed in the decay phase, while the third observation (N3) was made in the brief re-brightening period. In the first two observations, we found that both accretion rates ( $\dot{m}_d$  and  $\dot{m}_h$ ) decreased, though, in the third observation, the accretion rates marginally increased. The shock was found to move outward ( $93 r_s$  to  $113 r_s$ ), although the shock strength remained stable ( $\sim 2.80$ ).

In TCAF, the normalization is a function of mass of the BH, distance and inclination angle of the system, and is given by  $N_{\text{tcaf}} \sim (r_g^2/4\pi d^2) \cos i$ , where  $d$  is distance in 10 kpc and  $i$  is inclination angle. Thus ideally, one should find that the normalization is the same for all the observations. However, there could be some fluctuations due to measurement errors. Nevertheless, one could see a large deviation if a jet is present (Jana et al. 2017; Jana 2018; Chatterjee et al. 2019). In our analysis, we find  $N_{\text{tcaf}} \sim 1.62, 1.65$  and  $1.67$  for N1, N2 and N3, respectively. This indicates that either there is no jet or a compact jet exists with very low outflow rate. Indeed, Russell et al. (2018) observed a compact jet in the system. We calculated the mass outflow rate using equation (16) of Chakrabarti (1999). The ratio of mass outflow rate ( $\dot{M}_{\text{out}}$ ) to mass inflow rate (accretion rate,  $\dot{M}_{\text{in}} = \dot{m}_d + \dot{m}_h$ ) is given by  $r_{\dot{m}} = \frac{\dot{M}_{\text{out}}}{\dot{M}_{\text{in}}} = \frac{\theta_{\text{out}}}{\theta_{\text{in}}} \frac{R}{4} \left(\frac{R^2}{R-1}\right)^{3/2} \exp\left(\frac{3}{2} - \frac{R^2}{R-1}\right)$ , where  $\theta_{\text{out}}$  and  $\theta_{\text{in}}$  are the solid angles subtended by the outflow and inflow, respectively. Using the TCAF model fitted  $R$  and assuming  $\theta_{\text{out}} \sim \theta_{\text{in}}$ , we found that  $\dot{M}_{\text{out}} \sim$

$0.003\dot{M}_{\text{in}}$  during all three observations. Thus, the mass outflow rate is indeed very low and stable, hence, the TCAF model normalization is constant.

The hard X-ray emission is reprocessed by the Keplerian accretion disk and contributes to the Fe  $K\alpha$  emission line and reflection hump (Guilbert & Rees 1988; Lightman & White 1988; Fabian et al. 1989). In general, the reflection hump is observed around  $\sim 15 - 30$  keV. We studied the reflection feature of the spectra utilizing the convolution model `reflect`. We find that the reflection is weak with  $R_{\text{refl}} = 0.15, 0.22$  and  $0.25$  in N1, N2 and N3, respectively. Low accretion rate and location far from the Keplerian disk are responsible for the weak reflection.

### 4.3 Intrinsic Properties of the System

Mass of the BH is a free parameter in the TCAF model. Thus, we can estimate the mass of the BH from the spectral analysis with the TCAF model. The masses of several BHs are already estimated from the spectral analysis with the TCAF model (Molla et al. 2016; Chatterjee et al. 2016; Shang et al. 2019). The mass of MAXI J1813–095 was unknown; thus we kept the mass free during the spectral analysis. The mass of the BH was obtained as  $7.38, 7.44$  and  $7.40 M_{\odot}$  in N1, N2 and N3, respectively. We plot the variation of mass with  $\Delta\chi^2$  in Figure 7. Taking an average of three observations, we estimate the mass of the BH as  $7.41^{+1.47}_{-1.52} M_{\odot}$ , with 90% confidence, or simply,  $7.4 \pm 1.5 M_{\odot}$ .

The Fe  $K\alpha$  line is subjected to relativistic broadening if it is emitted from a region very close to the BH (Fabian et al. 1989; Laor 1991). In this work, we used relativistic model `LAOR` to fit the *NuSTAR* data for broad iron  $K\alpha$  emission line. In the process, we obtained the inner edge of the accretion flow ( $R_{\text{in}}$ ). Equating  $R_{\text{in}}$  with the innermost stable circular orbit ( $R_{\text{isco}}$ ), we can calculate the spin of the BH. In this method, the spins of several BHs have been estimated (Miller et al. 2004; Park et al. 2004; Reis et al. 2008; Mondal et al. 2016). For BHC MAXI J1813–095, we obtained the inner edge of the accretion flow  $R_{\text{in}}$  as  $2.64^{+0.10}_{-0.06} r_g$ ,  $2.59^{+0.11}_{-0.08} r_g$ , and  $2.58^{+0.11}_{-0.07} r_g$ , for N1, N2 and N3, respectively. This translates to the spin parameter ( $a^*$ ) of the BH as  $0.74^{+0.02}_{-0.03}$ ,  $0.75^{+0.02}_{-0.03}$  and  $0.76^{+0.02}_{-0.03}$  for N1, N2 and N3, respectively. The accretion flow moves closer to the BH in the soft state compared to the hard state. Since all the observations are taken in the hard state,  $R_{\text{in}}$  would have moved closer in the soft state. Hence, the estimated spin parameter ( $a^*$ ) only gives us the minimum value. Thus, we conclude the spin parameter of MAXI J1813–095 to be  $a^* > 0.76$ .

The strength of the reflection and the Fe line emission also depend on the inclination angle of the source. Thus, from the reflection and line emission, the inclination angle of the source can be constrained. We found evidence for weak reflection in all three observations. From the `reflect` model fitted parameter,  $\cos(\text{incl})$  varied between 0.71 and 0.88, which translates to  $\theta_{\text{incl}}$  between  $28.36^\circ$  and  $44.76^\circ$ . From `LAOR` model fitting, the  $\theta_{\text{incl}}$  is between  $31.88^\circ$  and  $36.26^\circ$ . Thus, the inclination angle of the source is  $28^\circ - 45^\circ$ . This low inclination angle naturally explains the low reflection of the source.

We also estimated the distance of the source from the unabsorbed flux and the Keplerian disk accretion rate. The source intrinsic luminosity,  $L = \eta\dot{M}c^2 = 4\pi d^2 F$ , where  $\eta$ ,  $\dot{M}$ ,  $c$ ,  $d$  and  $F$  are the accretion efficiency, mass accretion rate, light speed, source distance and unabsorbed flux, respectively. The Eddington luminosity,  $L_{\text{Edd}} = \eta\dot{M}_{\text{Edd}}c^2$ , where  $\dot{M}_{\text{Edd}}$  is the Eddington mass accretion rate. The TCAF model fitted mass accretion rate  $\dot{m} = \dot{M}/\dot{M}_{\text{Edd}}$ . From these three equations, we have  $4\pi d^2 F = \dot{m}L_{\text{Edd}}$ . From this equation, we estimated the distance from the three *NuSTAR* observations as 6.02 kpc, 5.83 kpc and 6.25 kpc, for N1, N2 and N3, respectively. From this, the source distance is about  $\sim 6$  kpc.

## 5 CONCLUSIONS

We studied the 2018 outburst of MAXI J1813–095 relying on data obtained from the *Swift*/XRT, *NICER* and *NuSTAR* observations. Our key findings are the following.

1. MAXI J1813–095 remained in the hard state during the entire outburst. The source did not show state transition. This makes the outburst a ‘failed’ outburst.
2. We investigated PDSs obtained from the 0.5 – 10 keV *NICER* light curves. Strong variabilities were identified with rms  $\sim 20\% - 30\%$ . We did not find any signature of QPO.
3. The 0.5 – 78 keV *Swift*/XRT+*NuSTAR* spectra can be fitted well with the combined `diskbb` and `powerlaw` model. However, the fitting improved when we added a reflection component (modeled with `reflect` in `XSPEC`). Weak reflection was found in the spectra obtained from all three observations.
4. From spectral analysis with the TCAF model, we extracted the accretion rates ( $\dot{m}_{\text{d}}$  and  $\dot{m}_{\text{h}}$ ), size of the Compton cloud (i.e., the shock location,  $X_{\text{s}}$ ) and shock compression ratio ( $R$ ). We observed that the accretion rates decreased and the shock moved outward in the decay phase as the outburst progressed.
5. We ascertained that the mass outflow rate is very low and constant during our observations.

6. We estimated the mass of MAXI J1813–095 as  $7.4 \pm 1.5 M_{\odot}$ . The distance of the source is estimated to be  $\sim 6$  kpc.
7. We estimated the spin parameter of the BH as  $a^* > 0.76$ . We also concluded that the inclination of the source is likely to be between  $28^{\circ} - 45^{\circ}$ .

**Acknowledgements** We thank the anonymous reviewer for the constructive review which improved the clarity of the manuscript. This research has made use of data and/or software provided by the High Energy Astrophysics Science Archive Research Center (HEASARC), which is a service of the Astrophysics Science Division at NASA/GSFC and the High Energy Astrophysics Division of the Smithsonian Astrophysical Observatory. This research has made use of the NuSTAR Data Analysis Software (NuSTARDAS) jointly developed by the ASI Science Data Center (ASDC, Italy) and California Institute of Technology (Caltech, USA). This work has made use of XRT data supplied by the UK Swift Science Data Centre at the University of Leicester, UK. A.J. and N.K. acknowledge support from the research fellowship from Physical Research Laboratory, Ahmedabad, India, funded by the Department of Space, Government of India for this work. K.C. acknowledges support from the DST/INSPIRE Fellowship (IF170233). R.B. acknowledges support from the CSIR-UGC NET qualified UGC fellowship (June-2018, 527223). Research by S.K.C. and D.D. is supported in part by the Higher Education Dept. of the Govt. of West Bengal, India. S.K.C. and D.D. also acknowledge partial support from ISRO sponsored RESPOND project (ISRO/RES/2/418/17-18) fund. H.-K. C. is supported by MOST of Taiwan under grants MOST/106-2923-M-007-002-MY3 and MOST/108-2112-M-007-003. D.D. acknowledges support from DST/GITA sponsored India-Taiwan collaborative project (GITA/DST/TWN/P-76/2017) fund.

## References

- Armas Padilla, M., Degenaar, N., Russell, D. M., & Wijnands, R. 2013, *MNRAS*, 428, 3083
- Armas Padilla, M., Muñoz-Darias, T., Sánchez-Sierras, J., et al. 2019, *MNRAS*, 485, 5235
- Arnaud, K. A. 1996, in *Astronomical Society of the Pacific Conference Series*, 101, *Astronomical Data Analysis Software and Systems V*, eds. G. H. Jacoby, & J. Barnes, 17
- Banerjee, A., Bhattacharjee, A., Debnath, D., & Chakrabarti, S. K. 2020, *RAA (Research in Astronomy and Astrophysics)*, 20, 208
- Belloni, T., Dieters, S., van den Ancker, M. E., et al. 1999, *ApJ*, 527, 345
- Bhowmick, R., Debnath, D., & Chatterjee, K., et al. *ApJ*, 2020 (submitted)
- Capitanio, F., Belloni, T., Del Santo, M., & Ubertini, P. 2009, *MNRAS*, 398, 1194
- Chakrabarti, S. K. 1990, *Theory of Transonic Astrophysical Flows* (World Scientific Publishing Co. Pte. Ltd., ISBN #9789814439220)
- Chakrabarti, S., & Titarchuk, L. G. 1995, *ApJ*, 455, 623
- Chakrabarti, S. K. 1996, *ApJ*, 464, 664
- Chakrabarti, S. K. 1997, *ApJ*, 484, 313
- Chakrabarti, S. K. 1999, *A&A*, 351, 185
- Chakrabarti, S. K., Mondal, S., & Debnath, D. 2015, *MNRAS*, 452, 3451
- Chakrabarti, S. K., Debnath, D., & Nagarkoti, S. 2019, *Advances in Space Research*, 63, 3749
- Chatterjee, D., Debnath, D., Chakrabarti, S. K., et al. 2016, *ApJ*, 827, 88
- Chatterjee, D., Debnath, D., Jana, A., & Chakrabarti, S. K. 2019, *Ap&SS*, 364, 14
- Chatterjee, K., Debnath, D., Chatterjee, D., et al. 2020, *MNRAS*, 493, 2452
- Debnath, D., Chakrabarti, S. K., & Mondal, S. 2014, *MNRAS*, 440, L121
- Debnath, D., Mondal, S., & Chakrabarti, S. K. 2015, *MNRAS*, 447, 1984
- Debnath, D., Jana, A., Chakrabarti, S. K., et al. 2017, *ApJ*, 850, 92
- Del Santo, M., Belloni, T. M., Tomsick, J. A., et al. 2016, *MNRAS*, 456, 3585
- Ebisawa, K., Titarchuk, L., & Chakrabarti, S. K. 1996, *PASJ*, 48, 59
- Esin, A. A., McClintock, J. E., & Narayan, R. 1997, *ApJ*, 489, 865
- Fabian, A. C., Rees, M. J., Stella, L., & White, N. E. 1989, *MNRAS*, 238, 729
- García, J. A., Tomsick, J. A., Sridhar, N., et al. 2019, *ApJ*, 885, 48
- Gendreau, K. C., Arzoumanian, Z., & Okajima, T. 2012, in *Society of Photo-Optical Instrumentation Engineers (SPIE) Conference Series*, 8443, *Space Telescopes and Instrumentation 2012: Ultraviolet to Gamma Ray*, eds. T. Takahashi, S. S. Murray, & J.-W. A. den Herder, 844313
- George, I. M., & Fabian, A. C. 1991, *MNRAS*, 249, 352
- Giri, K., & Chakrabarti, S. K. 2012, *MNRAS*, 421, 666
- Guilbert, P. W., & Rees, M. J. 1988, *MNRAS*, 233, 475
- Haardt, F., & Maraschi, L. 1993, *ApJ*, 413, 507
- Harrison, F. A., Craig, W. W., Christensen, F. E., et al. 2013, *ApJ*, 770, 103
- Homan, J., & Belloni, T. 2005, *Ap&SS*, 300, 107
- Jana, A. 2018, in *Exploring the Universe: From Near Space to Extra-Galactic*, ed. B. Mukhopadhyay & S. Sasmal, 53, 299
- Jana, A., Debnath, D., Chakrabarti, S. K., et al. 2016, *ApJ*, 819, 107

- Jana, A., Chakrabarti, S. K., & Debnath, D. 2017, *ApJ*, 850, 91
- Jana, A., Debnath, D., Chakrabarti, S. K., & Chatterjee, D. 2020a, *RAA (Research in Astronomy and Astrophysics)*, 20, 028
- Jana, A., Debnath, D., Chatterjee, D., et al. 2020b, *ApJ*, 897, 3
- Jana, A., Jaisawal, G. K., Naik, S., et al. 2021, arXiv:2104.13005
- Kawase, T., Negoro, H., Yoneyama, T., et al. 2018, *The Astronomer’s Telegram*, 11323, 1
- Kennea, J. A., Palmer, D. M., Lien, A. Y., et al. 2018, *The Astronomer’s Telegram*, 11326, 1
- Laor, A. 1991, *ApJ*, 376, 90
- Lightman, A. P., & White, T. R. 1988, *ApJ*, 335, 57
- Magdziarz, P., & Zdziarski, A. A. 1995, *MNRAS*, 273, 837
- Matt, G., Perola, G. C., & Piro, L. 1991, *A&A*, 247, 25
- Miller, J. M., Fabian, A. C., Reynolds, C. S., et al. 2004, *ApJL*, 606, L131
- Molla, A. A., Debnath, D., Chakrabarti, S. K., et al. 2016, *MNRAS*, 460, 3163
- Molteni, D., Sponholz, H., & Chakrabarti, S. K. 1996, *ApJ*, 457, 805
- Mondal, S., & Chakrabarti, S. K. 2019, *MNRAS*, 483, 1178
- Mondal, S., Chakrabarti, S. K., & Debnath, D. 2016, *Ap&SS*, 361, 309
- Mondal, S., Chakrabarti, S. K., Nagarkoti, S., & Arévalo, P. 2017, *ApJ*, 850, 47
- Nandi, P., Chakrabarti, S. K., & Mondal, S. 2019, *ApJ*, 877, 65
- Park, S. Q., Miller, J. M., McClintock, J. E., et al. 2004, *ApJ*, 610, 378
- Prigozhin, G., Gendreau, K., Foster, R., et al. 2012, in *SPIE Conference Series*, 8453, High Energy, Optical, and Infrared Detectors for Astronomy V, eds. A. D. Holland, & J. W. Beletic, 845318
- Rau, A. 2018, *The Astronomer’s Telegram*, 11332, 1
- Reis, R. C., Fabian, A. C., Ross, R. R., et al. 2008, *MNRAS*, 387, 1489
- Reis, R. C., Miller, J. M., Fabian, A. C., et al. 2011, *MNRAS*, 410, 2497
- Remillard, R. A., & McClintock, J. E. 2006, *ARA&A*, 44, 49
- Russell, T. D., Miller-Jones, J. C. A., Sivakoff, G. R., Tetarenko, A. J., & JACPOX XRB Collaboration, 2018, *The Astronomer’s Telegram*, 11356, 1
- Ryu, D., Chakrabarti, S. K., & Molteni, D. 1997, *ApJ*, 474, 378
- Shakura, N. I., & Sunyaev, R. A. 1973, *A&A*, 500, 33
- Shang, J. R., Debnath, D., Chatterjee, D., et al. 2019, *ApJ*, 875, 4
- Stiele, H., & Kong, A. K. H. 2018, *ApJ*, 868, 71
- Sturner, S. J., & Shrader, C. R. 2005, *ApJ*, 625, 923
- Sunyaev, R. A., & Titarchuk, L. G. 1980, *A&A*, 500, 167
- Tetarenko, B. E., Sivakoff, G. R., Heinke, C. O., & Gladstone, J. C. 2016, *ApJS*, 222, 15
- Wilms, J., Allen, A., & McCray, R. 2000, *ApJ*, 542, 914
- Zdziarski, A. A., Zycki, P. T., Svensson, R., & Boldt, E. 1993, *ApJ*, 405, 125